Maximum *a posteriori* natural scene reconstruction from retinal ganglion cells with deep denoiser priors

Eric G. Wu
Stanford University
wueric@stanford.edu

Nora Brackbill
Stanford University

Alexander Sher & Alan M. Litke
University of California, Santa Cruz

Eero P. Simoncelli
Flatiron Institute, Simons Foundation,
and New York University
eero.simoncelli@nyu.edu

E.J. Chichilnisky
Stanford University
ej@stanford.edu

Abstract

Visual information arriving at the retina is transmitted to the brain by signals in the optic nerve, and the brain must rely solely on these signals to make inferences about the visual world. Previous work has probed the content of these signals by directly reconstructing images from retinal activity using linear regression or nonlinear regression with neural networks. Maximum *a posteriori* (MAP) reconstruction using retinal encoding models and separately-trained natural image priors offers a more general and principled approach. We develop a novel method for approximate MAP reconstruction that combines a generalized linear model for retinal responses to light, including their dependence on spike history and spikes of neighboring cells, with the image prior implicitly embedded in a deep convolutional neural network trained for image denoising. We use this method to reconstruct natural images from *ex vivo* simultaneously-recorded spikes of hundreds of retinal ganglion cells uniformly sampling a region of the retina. The method produces reconstructions that match or exceed the state-of-the-art in perceptual similarity and exhibit additional fine detail, while using substantially fewer model parameters than previous approaches. The use of more rudimentary encoding models (a linear-nonlinear-Poisson cascade) or image priors (a $1/f$ spectral model) significantly reduces reconstruction performance, indicating the essential role of both components in achieving high-quality reconstructed images from the retinal signal.

1 Introduction

A torrent of visual information arrives at each of our eyes where it is transduced by a large population of photoreceptors and transformed by retinal circuitry. The resulting signals are transmitted to the brain in the spikes of a relatively small number of retinal ganglion cells (RGCs), suggesting that a large fraction of this visual information is lost. Elucidating the nature of these encoded signals, and the inference processes the brain could use to interpret them, is fundamental to understanding biological vision. Image reconstruction provides a method of visualizing the content encoded by RGC signals, evaluating it using standard image quality metrics, and reasoning about how the brain might use it [1, 2, 3, 4]. The fidelity and quality of reconstructed images also provides a useful objective function for optimizing the design of electrical stimulation patterns delivered by devices implanted to restore vision to people blinded by retinal degeneration [5, 6].

36th Conference on Neural Information Processing Systems (NeurIPS 2022).

The simplest and most well-studied image reconstruction method is linear regression [1, 3, 7]. Optimal reconstruction kernels are learned for each RGC using least-squares regression of recorded responses to many visual images, and the reconstruction of a new incident image is computed with the sum of the filters weighted by the measured response of each cell. The quality of linearly reconstructed images can be enhanced by applying an autoencoder neural network to impose natural image priors [8], or by using deep neural networks to non-linearly recover additional high spatial frequency image components [4]. Neural networks can also be directly trained (supervised) for reconstruction from raw data, but this is data-intensive, and has limited their use to simulated data, or low-dimensional stimuli and small numbers of cells [9]. These direct approaches leave substantial room for improvement and interpretation. A Bayesian formulation, in which encoding model and image priors are made explicit and are separately designed and optimized, offers a more flexible and interpretable solution.

Here, we present a method for approximate maximum *a posteriori* (MAP) image reconstruction from recorded RGC spikes, combining a retinal encoding model that accurately captures retinal responses [10] with state-of-the-art image priors that are implicitly embedded in deep denoising networks [11, 12, 13, 14, 15, 16]. Separating the contributions of image prior and RGC spiking response likelihood allows independent training of both elements, and offers flexible exploration and interpretation. Specifically, (1) any pre-trained or closed-form natural image prior can be used, and the effects of different priors can be compared; and (2) any model of RGC encoding that provides an explicit likelihood can be used, allowing examination of the relative importance of different model components in representing the visual signal, such as spike train history, cell-to-cell correlations and output nonlinearities. We apply our method to reconstruct flashed natural images from responses of several hundred macaque RGCs of identified types recorded with large-scale electrode arrays. We compare these results to published state-of-the-art linear and neural network regression methods. The new method matches or outperforms previous methods, producing sharper, more naturalistic reconstructions, and similar or greater perceptual similarity to ground truth. However, our method also produces some reconstructions with distinctive hallucinated image structure, as would be expected when RGC signals are noisy and image priors dominate the reconstruction process. Finally, comparisons to reconstructions using more conventional encoding models and image priors reveal that both aspects of the approach are important for the most accurate reconstructions. Source code, fitted models, and a subset of the test dataset used to produce example reconstructions are available at `https://github.com/wueric/RGC_MAP_reconstruction`.

2 Retinal data and stimuli

Extracellular recordings from RGCs in the peripheral macaque retina were performed *ex vivo* using a 512-electrode system [17] (see [3] for details). Retinas were obtained from terminally anesthetized macaque monkeys used by other laboratories, in accordance with Institutional Animal Care and Use Committee requirements. Spikes from individual RGCs were identified with the YASS [18] spike-sorter. A 30-minute spatio-temporal white noise stimulus [19] was used to compute spatio-temporal receptive fields, and to identify cells of distinct types. Analysis focused on the four major RGC types of the primate retina (ON parasol, OFF parasol, ON midget, and OFF midget) [20, 21], totaling roughly 700 cells per recording. The receptive fields [22] of all four cell types formed regular mosaics, with each providing nearly-complete coverage of a region of visual space (Figure 1B).

Natural images were presented to the retina as described previously [3]. Images from the ImageNet database [23] were converted to grayscale and cropped to 256x160. Each pixel measured approximately $11 \times 11\,\mu$m at the retina. Each stimulus image was displayed statically for 100 ms, followed by a 400 ms uniform gray display, allowing each image presentation to be treated as an independent trial (Figure 1A). Recordings were gathered from retinas of two animals, in response to 19,000 and 10,000 images, respectively. Details are summarized in Tables 4 and 5 in the Appendix.

3 MAP image reconstruction from RGC spikes

The MAP estimate of the stimulus image $\mathbf{x}$ (a vector of pixel luminances) from observed RGC spike trains $\mathbf{s}$ corresponds to the minimum of the negative log of the posterior distribution, $-\log p(\mathbf{x} \mid \mathbf{s})$, which can be expressed using Bayes' Rule as:

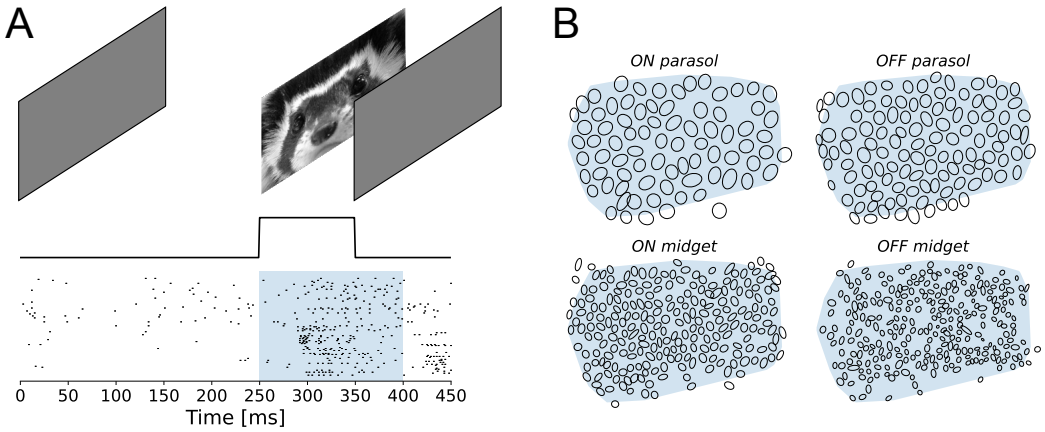

Figure 1: (A) Trial structure for a single stimulus image presentation. Static stimulus images are displayed for 100 ms, separated by 400 ms uniform gray display. Spikes occurring within 150 ms of the onset of the stimulus image, corresponding to the shaded blue region, were used to compute encoding negative log-likelihoods. (B) Receptive field mosaics from one retina for the four major RGC types (ON parasol, OFF parasol, ON midget, OFF midget) used in the image reconstructions. Image quality metrics were computed over the shaded blue region, to exclude areas of the image that were insufficiently covered by receptive fields of recorded RGCs.

$$\hat{\mathbf{x}}(\mathbf{s}) = \arg\min_{\mathbf{x}} \big\{ -\log p(\mathbf{s} \mid \mathbf{x}) - \log p(\mathbf{x}) \big\}. \tag{1}$$

The first term is the negative log likelihood of the stimulus, as obtained from an encoding model describing the probabilistic spiking of RGCs given a stimulus. In principle, any model can be used, and its parameters learned from experimentally measured RGC responses. The second term is the negative log prior of the stimulus which can be learned from natural images, independent of retinal responses. Because encoding models with varying levels of fidelity and detail can be mixed with priors of varying sophistication, the MAP approach allows us to probe the distinct roles of these two components in image reconstruction [24, 25].

3.1 RGC encoding models

Encoding models for each RGC must be fitted to the experimental data before performing MAP reconstruction. Two types of encoding models were used: (1) a linear-nonlinear-Poisson (LNP) cascade model with an exponential nonlinearity, the most commonly used model of RGC responses to visual stimuli [7]; and (2) a generalized linear model (GLM) that augments the LNP model with a feedback loop and cross-connections between neighboring cells, and which can accurately capture fine spike timing structure and cell-to-cell correlations [10]. Encoding models were fitted to a training partition of the data by minimizing the negative log-likelihood, and regularization hyperparameters were tuned by evaluating the negative log-likelihood on a test partition for a small subset of RGCs of each type.

Linear-nonlinear-Poisson (LNP) encoding model The LNP model is the *de facto* standard model for describing the probabilistic spiking of RGCs in response to visual stimuli [7]. The model parameters for each RGC consist of a linear spatial filter $\mathbf{m}$, and a scalar bias b. In the model, a scalar generator signal $\mathbf{m}^T\mathbf{x} + b$ is passed through an exponential nonlinearity to yield a spike rate $\lambda(\mathbf{x})$. Responses, s, are defined as the RGC spike count in a 150 ms interval, which are assumed to be Poisson-distributed with rate $\lambda(\mathbf{x})$. The resulting negative log-likelihood for each RGC is

$$-\log p(s \mid \mathbf{x}) = \exp\{\mathbf{m}^T\mathbf{x} + b\} - s(\mathbf{m}^T\mathbf{x} + b), \tag{2}$$

which is convex in $\mathbf{m}$ and b. In practice, to ensure that the spatial filters were spatially compact and corresponded approximately with receptive fields obtained using reverse correlation with white noise, the negative log-likelihood objective was augmented with two regularization terms: an L1 penalty to induce sparsity in the filter weights, and an L2 penalty to minimize the difference between the filter and the receptive field. The complete LNP-fitting objective function with both regularization terms is described in A.4. The parameters of each cell were optimized separately using FISTA [26].

MAP reconstruction requires the joint negative log-likelihood of the image based on the observed spikes from every RGC. Since the LNP model assumes that the responses for each cell are statistically independent, this is simply the sum of the single-cell negative log-likelihoods, which is convex in the image $\mathbf{x}$:

$$-\log p(\mathbf{s} \mid \mathbf{x}) = \sum_{i \in \text{Cells}} \exp\{\mathbf{m_i}^T \mathbf{x} + b_i\} - (\mathbf{m_i}^T \mathbf{x} + b_i). \tag{3}$$

Generalized linear encoding models The generalized linear model (GLM) is an augmentation of the LNP model that incorporates the effects of spiking history and cell-to-cell correlations on neural response [10]. In the GLM, the ith RGC is parameterized by a spatio-temporal stimulus filter $k_i[x, y, t]$, a feedback (spike history) filter $f_i[t]$, a set of neighboring cell coupling filters $c_i^{(j)}[t]$, and a bias b_i. The GLM was fitted to spike counts measured within 1 ms time bins, a duration approximately matched to the spike refractory period [27, 28], yielding binary spike counts. To limit the number of parameters and improve computational efficiency, the stimulus filter was assumed to be space-time separable $k_i[x, y, t] = \mathbf{m}_i[x, y]h_i[t]$. Letting $*$ denote time-domain convolution, $w[t]$ denote the time course of the stimulus (boxcar), and $\{i\}^C$ denote the set of coupled neighboring cells, the generator signal $g[t]$ is

$$g_i[t] = (\mathbf{m}_i^T \mathbf{x})(h_i * w)[t-1] + (s_i * f_i)[t-1] + \sum_{j \in \{i\}^C} (s_j * c_i^{(j)})[t-1] + b_i. \tag{4}$$

Assuming a sigmoidal nonlinearity $\sigma(x) = e^x/(1+e^x)$ and a Bernoulli spiking distribution, the negative log-likelihood used to fit a single cell (see A.5.2 for complete derivation) is

$$-\log p(s_i[N, ..., T] \mid \mathbf{x}, s_i[0, ..., N-1], \mathbf{s}_{\{i\}^C}[0, ..., T]) = \sum_{t=N}^{T} \big\{ \log(1 + \exp\{g_i[t]\}) - s_i[t] g_i[t] \big\}. \tag{5}$$

To simplify the GLM, the filters h_i, f_i, and $c_i^{(j)}$ were parameterized as weighted sums over a set of cosine-shaped "bump" functions [10] (discussed further in A.5.4). As with the LNP model, L1 and L2 regularization terms were added to constrain the spatial filters, and an additional $L_{1,2}$ group sparsity penalty was imposed on the coupling filters to eliminate spurious cell-to-cell correlations. The complete objective function is described in detail in A.5.3. Model parameters were found by alternating between convex minimization steps for the spatial and temporal filters of each RGC, using FISTA [26, 29] for each step.

For MAP image reconstruction, we compute the joint negative log-likelihood of the image based on responses of all cells over time bins $N, N+1, \ldots, T$. This can be constructed from the single cell negative log-likelihoods using the chain rule (see A.5.5 for derivation), and is again convex in the image $\mathbf{x}$:

$$-\log p(\mathbf{s}[N, ..., T] \mid \mathbf{x}, \mathbf{s}[0, ..., N-1]) = -\sum_{t=N}^{T} \sum_{i \in \text{cells}} \log p(s_i[t] \mid \mathbf{x}, s_i[0, ..., t-1], \mathbf{s}_{\{i\}^C}[0, ..., t-1]). \tag{6}$$

3.2 MAP with Gaussian $1/f$ priors

A stationary Gaussian prior with $1/f$ spectral energy is the simplest and most commonly used image prior [30], and is the basis for most classical image processing algorithms. The $1/f$ prior

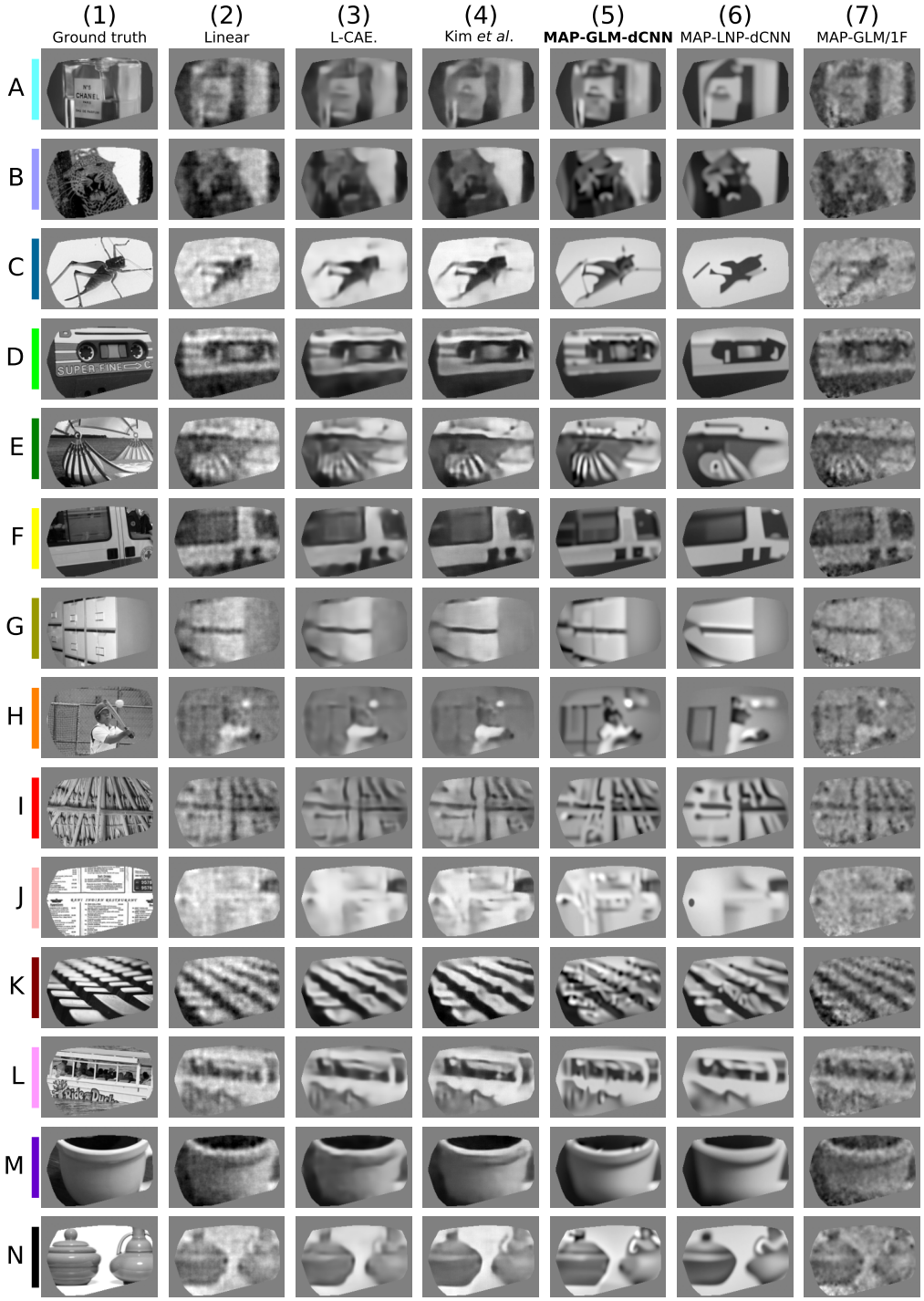

Figure 2: Selected stimulus images and reconstructions for the retina of Figure 1B. Images are masked to only include regions covered by recorded RGCs. Colors on the left correspond to the colored markers in the scatter plots in Figure 3. Column contents: (1) Ground truth stimulus image; (2) Linear reconstruction; (3) Linear reconstruction followed by CNN autoencoder (L-CAE, [8]); (4) Linear reconstruction followed by neural network regression [4]; (5) Our method, approximate MAP with GLM and denoiser prior (MAP-GLM-dCNN); (6) Approximate MAP with LNP encoder and denoiser prior (MAP-LNP-dCNN); (7) Exact MAP with GLM encoder and $1/f$ prior (MAP-GLM-1F).

assumes that pixels of the image are drawn from a stationary jointly Gaussian distribution (and thus that the spatial covariance matrix is diagonalized by the 2D Fourier basis) and that spectral power (variance of each spatial frequency component) falls off in inverse proportion to the square of the frequency f^2. Discarding terms that do not depend on the image $\mathbf{x}$, the negative log prior can be written as $-\log p(\mathbf{x}) = \sum_k |a_k(x)|^2/f_k^2$ where $a_k(x)$ is the amplitude of the kth Fourier coefficient at frequency f_k. MAP image reconstruction using this prior can be performed using standard unconstrained convex minimization methods because both the negative log prior and the RGC encoding negative log-likelihoods described in (3) and (6) are convex.

3.3 Approximate MAP with denoising convolutional neural network (dCNN) priors

Modern denoising convolutional neural networks can represent powerful image priors, but these priors are implicit [12, 31]: they are not expressed in closed form, and their values cannot be computed directly, making exact MAP inference difficult. The "plug-and-play" methodology provides an approximate iterative procedure for using such denoisers in MAP estimation problems [11], by incorporating them into variable-splitting optimization methods such as half-quadratic splitting (HQS) [32] or alternating direction method of multipliers (ADMM) [33, 34, 35]. Here, we use a method based on the HQS method presented in [15] to perform MAP reconstruction from RGC spikes. Following [15], we introduce an auxiliary variable $\mathbf{z}$, split the original problem in equation (1) into two complementary sub-problems, incorporate a regularization parameter λ_p to control the strength of the prior term, and iteratively alternate between solving the two sub-problems:

$$\mathbf{x}^{(k+1)} = \arg\min_{\mathbf{x}} \big\{ -\log p(\mathbf{s} \mid \mathbf{x}) + \frac{\rho^{(k)}}{2}|\mathbf{x} - \mathbf{z}^{(k)}|_2^2 \big\} \tag{7}$$

$$\mathbf{z}^{(k+1)} = \arg\min_{\mathbf{z}} \big\{ -\lambda_p \log p(\mathbf{z}) + \frac{\rho^{(k)}}{2}|\mathbf{z} - \mathbf{x}^{(k+1)}|_2^2 \big\}. \tag{8}$$

Since the sub-problem in equation (8) has the same objective function as MAP Gaussian denoising with known noise variance $\lambda_p/\rho^{(k)}$, we compute its solution using a single forward pass of a pre-trained DRUNet denoiser network [15]. This is an approximation, because the denoiser was trained with an MSE objective and hence targets the mean of the posterior rather than its maximum. The approximation is correct in the limit of small noise, and thus can be used within an iterative procedure that gradually decreases the objective function [11]. The overall iterative MAP reconstruction procedure is given in Algorithm 1.

Algorithm 1 Approximate MAP reconstruction from RGC spikes (MAP-*encoder*-dCNN)

Hyperparameters: λ_p, schedule $\rho^{(1)}$, $\rho^{(2)}$, ..., $\rho^{(N)}$
Inputs: observed spike count vector $\mathbf{s} \in \mathbb{R}^C$
Initialize $\mathbf{z}^{(1)}$ to linear solution
for $k \in 1, 2, ...K$ **do**
    $\mathbf{x}^{(k+1)} \leftarrow \arg\min_{\mathbf{x}} \big\{ -\log p(\mathbf{s} \mid \mathbf{x}) + \frac{\rho^{(k)}}{2}|\mathbf{x} - \mathbf{z}^{(k)}|_2^2 \big\}$
    $\mathbf{z}^{(k+1)} \leftarrow$Unblind-DRUNet-Denoiser($\mathbf{x}^{(k+1)}; \sigma^2 = \frac{\lambda_p}{\rho^{(k)}}$)
end for

Unlike most applications of HQS, the encoding term in equation (7) is non-quadratic in $\mathbf{x}$ and hence (7) was solved iteratively (gradient descent with momentum and backtracking line search) rather than in closed form. $\mathbf{z}^{(1)}$ was initialized as the linear solution; using random Gaussian initialization does not significantly affect the results (see Appendix A.6). Because convergence in the mathematical sense is not necessary for most imaging applications [36], $K = 25$ iterations were used in Algorithm 1. As in [15], $\rho^{(k)}$ was increased per-iteration on a log-spaced schedule. The hyperparameters λ_p and $[\rho^{(1)}, \rho^{(25)}]$ were determined by performing a grid search and evaluating reconstruction quality on an 80-image subset of the test partition. Variations in hyperparameters over a reasonable range ($\rho^{(1)} \in [10^{-2}, 10^{-1}]$, $\rho^{(25)} \in [30, 500]$, $\lambda_p \approx 0.1$) produced similar reconstruction quality, and optimal hyperparameters were similar across the two retinas and across LNP and GLM encoding models. Approximate MAP reconstructions using this algorithm are termed MAP-GLM-dCNN and MAP-LNP-dCNN for the GLM and LNP encoding models, respectively.

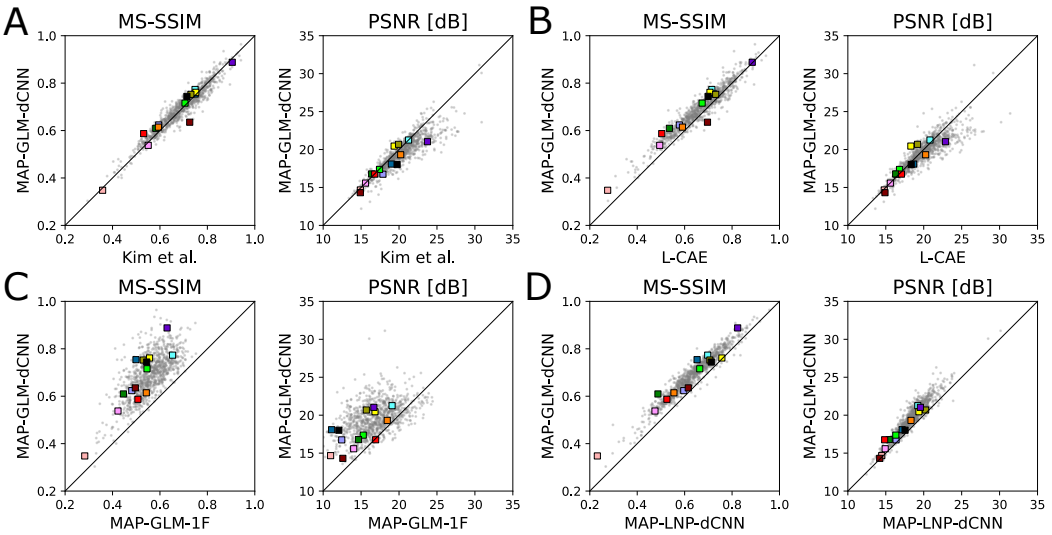

Figure 3: Comparisons of reconstruction quality of test data from spikes of the retina shown in Figure 1B. Each panel shows values of two metrics – multi-scale structural similarity (MS-SSIM) [37], and PSNR – for all test images (individual points). Colored markers correspond to the example images in Figure 2. Vertical axis of all graphs corresponds to our method (MAP-GLM-dCNN), and horizontal axis corresponds to other methods: (A) MAP-GLM-dCNN vs. Kim *et al.* linear with neural network regression [4]. MAP-GLM-dCNN achieves comparable perceptual similarity but worse PSNR (B) MAP-GLM-dCNN vs. L-CAE [8]. MAP-GLM-dCNN achieves improved perceptual similarity with slightly worse PSNR. (C) MAP-GLM-dCNN vs. MAP-GLM-1F. Reconstructions using the weaker $1/f$ prior have worse perceptual similarity and PSNR. (D) MAP-GLM-dCNN vs. MAP-LNP-dCNN. Reconstructions using the simpler LNP encoding model have worse perceptual similarity and PSNR.

3.4 Benchmark: nonlinear regression with artificial neural networks

Current state-of-the-art methods for reconstruction of natural images from RGC spikes rely on an initial linear reconstruction step [1, 3], followed by application of nonlinear neural networks to further improve the image. In one approach, Parthasarathy *et al.* [8] use a deep convolutional autoencoder (L-CAE) trained with MSE loss to incorporate image priors in the reconstruction. The authors trained and tested the model on simulated RGC spikes. For our comparisons, we used the published architecture and hyperparameters, but trained the model using backpropagation on experimentally measured retinal spike counts. Further details and characterization of the L-CAE on experimental data are provided in Appendix A.7. Another method was developed by Kim *et al.* [4], who partition the target image into high and low spatial frequency components. Linear regression from RGC spike counts is used to recover the low-frequency component, and a fully-connected neural network is used to non-linearly reconstruct the high-frequency component. The two components are summed and then passed through a final deblurring CNN. Both the high-frequency network and the deblurring CNN are trained with backpropagation on RGC responses to natural images. This method has achieved the most accurate reconstructions in the literature to date. Details of our implementation of the Kim *et al.* method are provided in Appendix A.8.

4 Results

4.1 Approximate MAP with GLM/dCNN matches or exceeds state-of-the-art results

To compare our MAP-GLM-dCNN method to current state-of-the-art approaches, image reconstructions were generated from the test partitions of the datasets. Example reconstructions are shown in columns 3-5 of Figure 2 for the L-CAE [8], for Kim *et al.* [4], and for our method, respectively. Qualitatively, the MAP-GLM-dCNN reconstructions are seen to be sharper than those of L-CAE, and contain additional image details (especially extended contours, as in rows C, E, G, H, I, L). When

Table 1: Average test and heldout MS-SSIM for each reconstruction method and retina.

	L-CAE		Kim *et al.*		**MAP-GLM-dCNN**		MAP-LNP-dCNN		MAP-GLM-1F	
	test	held	test	held	test	held	test	held	test	held
Retina 1	0.665	0.661	0.687	0.681	**0.689**	**0.688**	0.635	0.636	0.557	0.552
Retina 2	0.643	0.645	**0.675**	**0.675**	0.668	0.673	0.601	0.609	0.584	0.577

Table 2: Average test and heldout PSNR for each reconstruction method and retina.

	L-CAE		Kim *et al.*		**MAP-GLM-dCNN**		MAP-LNP-dCNN		MAP-GLM-1F	
	test	held	test	held	test	held	test	held	test	held
Retina 1	19.9	20.1	**20.2**	**20.5**	19.5	19.5	18.3	18.4	16.8	16.8
Retina 2	19.3	19.6	**19.8**	**20.1**	18.5	18.5	17.0	17.1	17.3	17.2

compared to Kim *et al.*, MAP-GLM-dCNN tended to recover more content, particularly straight edges (rows E, G, H, I, L), but sometimes exaggerated contrast (rows H, I, N). MAP-GLM-dCNN produced qualitatively different artifacts than the other methods. In particular, it sometimes hallucinated naturalistic structure not present in the stimulus images (rows J, K, N), including striking irregularities in contours (rows D, K, L, M).

Reconstruction quality for each method was quantified over the test and heldout partitions using MS-SSIM and PSNR. Scatter plots comparing MS-SSIM and PSNR on the test partition of one retina are shown in Figure 3A and 3B for Kim *et al.* and the L-CAE, respectively, and summary statistics over the test and held out partitions for both retinas are presented in Tables 1 and 2. On a per-image basis, the perceptual similarity (measured with MS-SSIM) of MAP-GLM-dCNN reconstructions to ground truth is higher than L-CAE (3B). The perceptual similarity of MAP-GLM-dCNN results is comparable to that of the much more complicated Kim *et al.* method (3A). But note that the PSNR of MAP-GLM-dCNN reconstructions was systematically lower than either benchmark. This is not surprising, as the MAP optimization procedure does not necessarily minimize MSE. These results held for both retinas (Tables 1 and 2).

4.2 Deep denoiser prior substantially improves image quality over $1/f$ prior

To test the importance of the image prior, MAP-GLM-dCNN results were compared against reconstruction using the GLM encoding model with the classical $1/f$ Gaussian prior (MAP-GLM-1F). Example reconstructed images using the denoiser prior and $1/f$ prior are shown in columns 5 and 7, respectively, of Figure 2. Images reconstructed with the denoiser prior are less "grainy", and tend to have both crisper edges and smoother surfaces. The artifacts seen in the $1/f$ examples are expected, since this simple prior does not constrain phase, whose alignment is essential for generating sharp spatially-localized features. Scatter plots of image quality on the test partition using MS-SSIM and PSNR are shown for one retina in Figure 3C, and mean values for both retinas are summarized in Tables 1 and 2. Consistent with the visual appearance, PSNR and MS-SSIM were systematically higher when using the denoiser prior, in both retinas. Thus, using the more sophisticated denoiser image prior substantially increased the perceptual similarity of the reconstructions to ground truth.

4.3 GLM encoding model recovers additional image structure over LNP encoding model

To test the importance of the encoding model, we compared images reconstructed using the GLM and LNP encoding models, both in combination with the the denoiser prior. Example images are shown in columns 5 and 6 of Figure 2. Images reconstructed using both models exhibit natural image structure, including smooth surfaces and well-defined edges, but the GLM-reconstructed images tended to have more realistic-looking textures, whereas the LNP-reconstructed images tended to be overly simplified. Moreover, the GLM method recovered more fine details (e.g., the legs of the insect in row C, the horizontal stripes on the tape cassette in row D, and the details on the hammock in row E, and the structure on the file cabinets in row G). The quality of image reconstructions for each image-response pair in the test partition for one retina were compared using MS-SSIM and PSNR in Figure 3D, and their mean values over the test and held out partitions for both retinas are summarized in Tables 1 and 2. In both retinas, images reconstructed using the GLM encoding model had systematically higher

MS-SSIM scores, indicating greater perceptual similarity to ground truth, than those reconstructed using the LNP encoding model. This demonstrates that the choice of encoding model significantly affects reconstruction quality, and that the inclusion of temporal spike dependencies and cell-to-cell correlations in the more sophisticated GLM encoding model provides important constraints on the visual signal encoded by the RGC spikes. This finding is consistent with previous work showing that decoding using the GLM (without priors) can access more information than simplified models lacking the cell-to-cell correlations or spiking history [10].

Table 3: Number of parameters trained on retinal data for each method (for retina 1). MAP-GLM-dCNN and L-CAE have comparable numbers of parameters. Because of sparsity regularization in the GLM spatial encoding filters, more than half (55%) of the parameters in the GLM model are zero. The Kim *et al.* model contains nearly an order-of-magnitude more parameters than either MAP-GLM-dCNN or L-CAE.

	L-CAE	Kim *et al.*	**MAP-GLM-dCNN**	MAP-LNP-dCNN	MAP-GLM-1F
Trained params.	$3.07 \cdot 10^7$	$2.44 \cdot 10^8$	$2.88 \cdot 10^7$	$2.85 \cdot 10^7$	$2.88 \cdot 10^7$

5 Discussion

We have presented a novel approximate MAP method for reconstructing natural images from the simultaneously recorded spikes of several hundred retinal ganglion cells, using an accurate probabilistic model of retinal encoding and a natural image prior implicit in a pre-trained denoising neural network. The method matches or outperforms the current state-of-the-art in terms of recovering naturalistic image structure and/or the perceptual similarity of reconstructions to ground truth, while also being more principled and interpretable due to the explicit Bayesian separation of the encoding model and prior. The new approach uses substantially fewer parameters than previous state-of-the-art methods based on neural networks, and does not require training neural networks on retinal data (the prior is obtained from a network trained exclusively on image denoising). We showed that both encoding model and image prior contributed to the high-quality image reconstructions: simplification of either substantially degraded performance. Thus, we expect that cell-to-cell correlations and temporal structure of spike trains, as well as sophisticated image priors, will prove important in understanding how the retinal signal is used by the brain.

Several previous studies have used GLM encoding models for stimulus reconstruction from experimentally-recorded retinal signals, revealing the significance of cell-to-cell correlations for decoding temporal structure in white noise stimuli [10, 38], and the significance of the temporal structure of spike trains in tracking moving features [2]. By including a complex natural image prior into a Bayesian reconstruction method, the present work more efficiently leverages both the GLM model and the experimental data to produce state-of-the-art natural image reconstructions.

The enhanced reconstructions and interpretability obtained with our method could lead to improved function of retinal implants for restoring vision. Previous work [5] has suggested that electrical stimulation with a retinal implant can be guided by minimizing the expected MSE of linearly reconstructed images. This method ignored fine temporal structure in RGC spike trains, and assumed that image priors captured by linear regression are sufficient for high performance. The method presented here offers an alternative approach to choosing simulation patterns to produce higher-fidelity artificial vision, while potentially being more robust than neural network methods. However, achieving this in real time with minimal latency presents a substantial technical challenge.

Our Bayesian reconstruction methodology relied on the convexity of the GLM encoding model, which allows for robust convergence. It is worthwhile to consider generalizations that might be used to evaluate more complex encoding models that are non-convex in the stimulus, such as subunit models [39, 40, 41] or artificial neural network retinal models[42, 43]. We are currently working on methods based on score-based sampling methods [44, 14] to answer this question.

Though the present work is limited to reconstruction of flashed static natural images from RGC spikes, extensions of the method could be used to probe how neurons encode visual information under more natural conditions. For example, a central problem is understanding how the visual system achieves high-acuity perception in the presence of "jitter" in eye position, even during fixation [45]. Previous computational efforts have probed this question, but have been largely limited to simulated data with

simple encoding models and stimuli [46, 47, 48]. Combining the methods put forth here with modern algorithms for image deblurring and motion-correction [49, 15] could yield more powerful methods to decode images from jittered retinal inputs. A related problem is understanding how the retina encodes the information contained in complex naturalistic movies [2], including movement of objects within a scene and other non-rigid transformations over time. The dimensionality of such stimuli and the consequent data requirements are high, so the use of machine learning methods to capture spatio-temporal priors [50, 51] separately from the retinal data will be important for understanding reconstruction in these contexts.

6 Funding

National Defense Science and Engineering Graduate (NDSEG) Fellowship (EGW), NSF IGERT 0801700 (NB), Wu Tsai Neurosciences Institute Big Ideas award, NSF CRCNS grant 1430348 (EJC/EPS), and NIH grants EY017992 and EY029247 (EJC).

References

[1] D. K. Warland, P. Reinagel, and M. Meister, "Decoding Visual Information From a Population of Retinal Ganglion Cells," *Journal of Neurophysiology*, vol. 78, pp. 2336–2350, Nov. 1997.

[2] V. Botella-Soler, S. Deny, G. Martius, O. Marre, and G. Tkačik, "Nonlinear decoding of a complex movie from the mammalian retina," *PLOS Computational Biology*, vol. 14, p. e1006057, May 2018.

[3] N. Brackbill, C. Rhoades, A. Kling, N. P. Shah, A. Sher, A. M. Litke, and E. Chichilnisky, "Reconstruction of natural images from responses of primate retinal ganglion cells," *eLife*, vol. 9, p. e58516, Nov. 2020.

[4] Y. J. Kim, N. Brackbill, E. Batty, J. Lee, C. Mitelut, W. Tong, E. J. Chichilnisky, and L. Paninski, "Nonlinear Decoding of Natural Images From Large-Scale Primate Retinal Ganglion Recordings," *Neural Computation*, vol. 33, pp. 1719–1750, June 2021.

[5] N. P. Shah, S. Madugula, L. Grosberg, G. Mena, P. Tandon, P. Hottowy, A. Sher, A. Litke, S. Mitra, and E. Chichilnisky, "Optimization of Electrical Stimulation for a High-Fidelity Artificial Retina," in *2019 9th International IEEE/EMBS Conference on Neural Engineering (NER)*, (San Francisco, CA, USA), pp. 714–718, IEEE, Mar. 2019.

[6] N. P. Shah and E. J. Chichilnisky, "Computational challenges and opportunities for a bi-directional artificial retina," *Journal of Neural Engineering*, vol. 17, p. 055002, Oct. 2020.

[7] F. Rieke, D. Warland, R. de Ruyter van Steveninck, and W. Bialek, *Spikes: Exploring the Neural Code*. Cambridge, MA, USA: MIT Press, 1999.

[8] N. Parthasarathy, E. Batty, W. Falcon, T. Rutten, M. Rajpal, E. Chichilnisky, and L. Paninski, "Neural Networks for Efficient Bayesian Decoding of Natural Images from Retinal Neurons," conference, Neuroscience, June 2017.

[9] Y. Zhang, S. Jia, Y. Zheng, Z. Yu, Y. Tian, S. Ma, T. Huang, and J. K. Liu, "Reconstruction of natural visual scenes from neural spikes with deep neural networks," *Neural Networks*, vol. 125, pp. 19–30, May 2020.

[10] J. W. Pillow, J. Shlens, L. Paninski, A. Sher, A. M. Litke, E. J. Chichilnisky, and E. P. Simoncelli, "Spatio-temporal correlations and visual signalling in a complete neuronal population," *Nature*, vol. 454, pp. 995–999, Aug. 2008.

[11] S. V. Venkatakrishnan, C. A. Bouman, and B. Wohlberg, "Plug-and-Play priors for model based reconstruction," in *2013 IEEE Global Conference on Signal and Information Processing*, (Austin, TX, USA), pp. 945–948, IEEE, Dec. 2013.

[12] Y. Romano, M. Elad, and P. Milanfar, "The Little Engine That Could: Regularization by Denoising (RED)," *SIAM Journal on Imaging Sciences*, vol. 10, pp. 1804–1844, Jan. 2017.

[13] Y. Song and S. Ermon, "Generative modeling by estimating gradients of the data distribution," in *Advances in Neural Information Processing Systems 32*, pp. 11918–11930, Curran Associates, Inc., 2019.

[14] Z. Kadkhodaie and E. P. Simoncelli, "Stochastic Solutions for Linear Inverse Problems using the Prior Implicit in a Denoiser," in *Advances in Neural Information Processing Systems 34 (NeurIPS 2021)*, p. 13, 2021.

[15] K. Zhang, Y. Li, W. Zuo, L. Zhang, L. Van Gool, and R. Timofte, "Plug-and-Play Image Restoration with Deep Denoiser Prior," *IEEE Transactions on Pattern Analysis and Machine Intelligence*, pp. 1–1, 2021.

[16] B. Kawar, G. Vaksman, and M. Elad, "Stochastic image denoising by sampling from the posterior distribution," tech. rep., aug 2021.

[17] A. Litke, N. Bezayiff, E. Chichilnisky, W. Cunningham, W. Dabrowski, A. Grillo, M. Grivich, P. Grybos, P. Hottowy, S. Kachiguine, R. Kalmar, K. Mathieson, D. Petrusca, M. Rahman, and A. Sher, "What does the eye tell the brain?: Development of a system for the large-scale recording of retinal output activity," *IEEE Transactions on Nuclear Science*, vol. 51, pp. 1434–1440, Aug. 2004.

[18] J. Lee, C. Mitelut, H. Shokri, I. Kinsella, N. Dethe, S. Wu, K. Li, E. B. Reyes, D. Turcu, E. Batty, Y. J. Kim, N. Brackbill, A. Kling, G. Goetz, E. Chichilnisky, D. Carlson, and L. Paninski, "YASS:

Yet Another Spike Sorter applied to large-scale multi-electrode array recordings in primate retina," preprint, Neuroscience, Mar. 2020.

[19] E. J. Chichilnisky, "A simple white noise analysis of neuronal light responses," *Network: Computation in Neural Systems*, vol. 12, pp. 199–213, 2001.

[20] E. J. Chichilnisky and R. S. Kalmar, "Functional Asymmetries in ON and OFF Ganglion Cells of Primate Retina," *The Journal of Neuroscience*, vol. 22, pp. 2737–2747, Apr. 2002.

[21] D. Dacey, "The mosaic of midget ganglion cells in the human retina," *The Journal of Neuroscience*, vol. 13, pp. 5334–5355, Dec. 1993.

[22] J. L. Gauthier, G. D. Field, A. Sher, M. Greschner, J. Shlens, A. M. Litke, and E. J. Chichilnisky, "Receptive Fields in Primate Retina Are Coordinated to Sample Visual Space More Uniformly," *PLoS Biology*, vol. 7, p. e1000063, Apr. 2009.

[23] L. Fei-Fei, J. Deng, and K. Li, "ImageNet: Constructing a large-scale image database," *Journal of Vision*, vol. 9, pp. 1037–1037, Aug. 2009.

[24] T. Naselaris, R. J. Prenger, K. N. Kay, M. Oliver, and J. L. Gallant, "Bayesian Reconstruction of Natural Images from Human Brain Activity," *Neuron*, vol. 63, pp. 902–915, Sept. 2009.

[25] L.-Q. Zhang, N. P. Cottaris, and D. H. Brainard, "An image reconstruction framework for characterizing initial visual encoding," *eLife*, vol. 11, p. e71132, Jan. 2022.

[26] A. Beck and M. Teboulle, "A Fast Iterative Shrinkage-Thresholding Algorithm for Linear Inverse Problems," *SIAM Journal on Imaging Sciences*, vol. 2, pp. 183–202, Jan. 2009.

[27] M. J. Berry and M. Meister, "Refractoriness and Neural Precision," *The Journal of Neuroscience*, vol. 18, pp. 2200–2211, Mar. 1998.

[28] V. J. Uzzell and E. J. Chichilnisky, "Precision of Spike Trains in Primate Retinal Ganglion Cells," *Journal of Neurophysiology*, vol. 92, pp. 780–789, Aug. 2004.

[29] J. Liu, S. Ji, and J. Ye, "Multi-Task Feature Learning Via Efficient 2,1-Norm Minimization," in *Proceedings of the Twenty-Fifth Conference on Uncertainty in Artificial Intelligence*, p. 10, 2009.

[30] E. P. Simoncelli, "Statistical Modeling of Photographic Images," in *Handbook of Image and Video Processing*, pp. 431–441, Elsevier, 2005.

[31] Z. Kadkhodaie and E. P. Simoncelli, "Solving linear inverse problems using the prior implicit in a denoiser," *arXiv*, July 2020.

[32] D. Geman and Chengda Yang, "Nonlinear image recovery with half-quadratic regularization," *IEEE Transactions on Image Processing*, vol. 4, pp. 932–946, July 1995.

[33] S. H. Chan, X. Wang, and O. A. Elgendy, "Plug-and-Play ADMM for Image Restoration: Fixed-Point Convergence and Applications," *IEEE Transactions on Computational Imaging*, vol. 3, pp. 84–98, Mar. 2017.

[34] A. M. Teodoro, J. M. Bioucas-Dias, and M. A. T. Figueiredo, "Image Restoration and Reconstruction using Targeted Plug-and-Play Priors," *IEEE Transactions on Computational Imaging*, vol. 5, pp. 675–686, Dec. 2019.

[35] Y. Sun, Z. Wu, X. Xu, B. Wohlberg, and U. Kamilov, "Scalable Plug-and-Play ADMM With Convergence Guarantees," *IEEE Transactions on Computational Imaging*, vol. 7, pp. 849–863, 2021.

[36] S. Diamond, V. Sitzmann, F. Heide, and G. Wetzstein, "Unrolled Optimization with Deep Priors," *arXiv:1705.08041 [cs]*, Dec. 2018. arXiv: 1705.08041.

[37] Z. Wang, A. Bovik, H. Sheikh, and E. Simoncelli, "Image Quality Assessment: From Error Visibility to Structural Similarity," *IEEE Transactions on Image Processing*, vol. 13, pp. 600–612, Apr. 2004.

[38] K. Ruda, J. Zylberberg, and G. D. Field, "Ignoring correlated activity causes a failure of retinal population codes," *Nature Communications*, vol. 11, p. 4605, Dec. 2020.

[39] J. Freeman, G. D. Field, P. H. Li, M. Greschner, D. H. Gunning, K. Mathieson, A. Sher, A. M. Litke, L. Paninski, E. P. Simoncelli, and E. J. Chichilnisky, "Mapping nonlinear receptive field subunits in primate retina at single cone resolution," *eLife*, vol. 4:e05241, Oct 2015.

[40] J. K. Liu, H. M. Schreyer, A. Onken, F. Rozenblit, M. H. Khani, V. Krishnamoorthy, S. Panzeri, and T. Gollisch, "Inference of neuronal functional circuitry with spike-triggered non-negative matrix factorization," *Nature Communications*, vol. 8, p. 149, Dec. 2017.

[41] N. P. Shah, N. Brackbill, C. Rhoades, A. Kling, G. Goetz, A. M. Litke, A. Sher, E. P. Simoncelli, and E. Chichilnisky, "Inference of nonlinear receptive field subunits with spike-triggered clustering," *eLife*, vol. 9, p. e45743, Mar. 2020.

[42] E. Batty, J. Merel, N. Brackbill, A. Heitman, A. Sher, A. Litke, E. J. Chichilnisky, and L. Paninski, "Multilayer recurrent network models of primate retinal ganglion cell responses," in *International Conference on Learning Representations 2017*, p. 12, 2017.

[43] L. McIntosh, N. Maheswaranathan, A. Nayebi, S. Ganguli, and S. Baccus, "Deep Learning Models of the Retinal Response to Natural Scenes," in *Advances in Neural Information Processing Systems 29 (NeurIPS 2016)*, p. 9, 2016.

[44] Y. Song, L. Shen, L. Xing, and S. Ermon, "Solving inverse problems in medical imaging with score-based generative models," in *International Conference on Learning Representations*, 2022.

[45] M. Rucci and M. Poletti, "Control and Functions of Fixational Eye Movements," *Annual Review of Vision Science*, vol. 1, pp. 499–518, Nov. 2015.

[46] X. Pitkow, H. Sompolinsky, and M. Meister, "A Neural Computation for Visual Acuity in the Presence of Eye Movements," *PLoS Biology*, vol. 5, p. e331, Dec. 2007.

[47] Y. Burak, U. Rokni, M. Meister, and H. Sompolinsky, "Bayesian model of dynamic image stabilization in the visual system," *Proceedings of the National Academy of Sciences*, vol. 107, pp. 19525–19530, Nov. 2010.

[48] A. G. Anderson, K. Ratnam, A. Roorda, and B. A. Olshausen, "High-acuity vision from retinal image motion," *Journal of Vision*, vol. 20, p. 34, July 2020.

[49] Y. Li, M. Tofighi, J. Geng, V. Monga, and Y. C. Eldar, "Efficient and Interpretable Deep Blind Image Deblurring Via Algorithm Unrolling," *IEEE Transactions on Computational Imaging*, vol. 6, pp. 666–681, 2020.

[50] A. Brifman, Y. Romano, and M. Elad, "Unified Single-Image and Video Super-Resolution via Denoising Algorithms," *IEEE Transactions on Image Processing*, vol. 28, pp. 6063–6076, Dec. 2019.

[51] D. Y. Sheth*, S. Mohan*, J. L. Vincent, R. Manzorro, P. A. Crozier, M. M. Khapra, E. P. Simoncelli, and C. Fernandez-Granda, "Unsupervised deep video denoising," in *Int'l Conf. Computer Vision (ICCV)*, Oct 2021.

[52] A. Paszke, S. Gross, F. Massa, A. Lerer, J. Bradbury, G. Chanan, T. Killeen, Z. Lin, N. Gimelshein, L. Antiga, A. Desmaison, A. Kopf, E. Yang, Z. DeVito, M. Raison, A. Tejani, S. Chilamkurthy, B. Steiner, L. Fang, J. Bai, and S. Chintala, "Pytorch: An imperative style, high-performance deep learning library," in *Advances in Neural Information Processing Systems 32* (H. Wallach, H. Larochelle, A. Beygelzimer, F. d'Alché-Buc, E. Fox, and R. Garnett, eds.), pp. 8024–8035, Curran Associates, Inc., 2019.

[53] D. P. Kingma and J. Ba, "Adam: A Method for Stochastic Optimization," in *3rd International Conference on Learning Representations*, 2015. arXiv: 1412.6980.

[54] O. Kupyn, T. Martyniuk, J. Wu, and Z. Wang, "DeblurGAN-v2: Deblurring (Orders-of-Magnitude) Faster and Better," in *2019 IEEE/CVF International Conference on Computer Vision (ICCV)*, (Seoul, Korea (South)), pp. 8877–8886, IEEE, Oct. 2019.

[55] K. Simonyan and A. Zisserman, "Very Deep Convolutional Networks for Large-Scale Image Recognition," in *International Conference on Learning Representations 2015*, Apr. 2015. arXiv: 1409.1556.

A Appendix

A.1 Potential negative impacts

A potential negative impact of any animal research is use of the animals. In the present work, eyes were obtained from animals that were euthanized in the course of experiments already being performed by other laboratories. If the eyes had not been used for these recordings, they would have been discarded. We are unaware of any other significant potential negative impacts.

A.2 Summary of experimental datasets

Table 4: Size (number of stimuli) of dataset partitions

	Train	Test	Heldout
Retina 1	17,500	1000	500
Retina 2	9000	500	500

Table 5: Cell counts for each dataset

	Total RGC count	ON parasol	OFF parasol	ON midget	OFF midget
Retina 1	695	79	115	228	273
Retina 2	778	97	130	207	344

A.3 Computational resources

All computations were performed using Pytorch [52] on a single NVIDIA V100 GPU with 32 GB of VRAM. Fitting encoding models for all cells in a single retina required approximately 24 hours of computational time.

A.4 Linear-nonlinear-Poisson (LNP) model and fitting

The LNP response model for a single RGC is

$$p(s|\mathbf{x}) \sim \text{Poiss}\left(\exp(\mathbf{m}^T\mathbf{x} + b)\right). \tag{9}$$

To fit this model to spike count data, we optimize the parameters $\mathbf{m}$ (the spatial stimulus filter) and b (the scalar bias) according to:

$$\arg\min_{\mathbf{m},b} \left\{ \exp\{\mathbf{m}^T\mathbf{x} + b\} - s(\mathbf{m}^T\mathbf{x} + b) + \gamma_1|\mathbf{m}|_1 + \frac{\gamma_2}{2}|\mathbf{m} - \mathbf{m}'|_2^2 \right\}. \tag{10}$$

The first two terms correspond to the negative log-likelihood of the model of equation (9). The third term is an L1 sparsity-inducing penalty on the spatial filter $\mathbf{m}$. The fourth term is an L2 penalty that induces similarity to $\mathbf{m}'$, which is an initial fit of the spatial filter obtained using reverse correlation with white noise. Together, the two regularization terms help to ensure that the spatial filters are spatially compact, contiguous, and resemble the white noise receptive fields. The hyperparameters for this objective function were optimized by performing a grid search and evaluating the log-likelihood of the responses of a small number of RGCs of each type in test partition. Optimization problems were solved separately for each RGC using FISTA [26].

A.5 Generalized linear model (GLM) and fitting

The GLM model of RGCs augments the LNP model to include feedback and coupling filters to account for refractoriness, bursting, and cell-to-cell correlations [10]. We make the following definitions and assumptions:

- The spikes for each RGC are binned into $T+1$ total time bins indexed as $t \in [0, 1, \ldots T-1, T]$ The stimulus onset (transition from gray screen to presented image) occurs at time $t = N$.
- The time bin durations are sufficiently brief (1 ms) that at most one spike per RGC can occur in any bin.
- The spike train for the ith single RGC is denoted s_i. The spike trains for a set of RGCs A is denoted $\mathbf{s}_A$, and the spike trains for the set of all RGCs except cell i is referred to as $\mathbf{s}_{\{i\}^C}$
- The visual stimulus within each trial is space-time separable, because each trial consists of a single statically-flashed image. In particular, the visual stimulus $v[x, y, t] = w[t]\mathbf{x}$ where $\mathbf{x}$ is the stimulus image, and $w[t]$ is a boxcar corresponding to the time component of the stimulus.

A.5.1 GLM with Bernoulli spiking

We assume that the spatio-temporal stimulus filter for the RGC is space-time separable. The GLM for the ith cell thus the following parameters:

- The spatial component of the stimulus filter $\mathbf{m}_i$
- The temporal component of the stimulus filter $h_i[t]$, assumed causal
- The additive (bias) constant b_i
- A feedback (spike history) filter $f_i[t]$, assumed causal
- Coupling filters for the neighboring RGCs, $c_i^{(j)}[t]$, assumed causal. The set of cells coupled to cell i is denoted $\{i\}^C$

Approximate nearest-neighbor distances for each of the cell types (ON parasol, OFF parasol, ON midget, OFF midget) were computed based on the reverse-correlation receptive field centers. Coupled neighbors consisted of cells within a multiple of the median nearest neighbor distances for each respective cell type (2 times the median nearest neighbor distance for parasols, 2.5 times the median nearest neighbor distance for midgets).

The generator signal of the ith RGC, which determines its instantaneous spiking probability, is defined as

$$g_i[t] = (\mathbf{m}_i^T \mathbf{x})(h_i * w)[t-1] + (s_i * f_i)[t-1] + \sum_{j \in \{i\}^C} (s_j * c_i^{(j)})[t-1] + b_i. \tag{11}$$

Since filters h_i, f_i, and $c_i^{(j)}$ are causal, $g_i[t]$ depends only on the stimulus and spikes that occur before time t.

The generator signal is passed through a sigmoidal nonlinearity $p[t] = \exp\{g_i[t]\}/(1 + \exp\{g_i[t]\})$, and a spike is generated with this probability. The log-likelihood of observing $s_0[t]$ spikes from cell i at time t given the stimulus and previously observed spikes is

$$\log p(s_i[t] \mid \mathbf{x}, s_i[0, \ldots, t-1], \mathbf{s}_{\{i\}^C}[0, \ldots, t-1]) = s_i[t] g_i[t] - \log(1 + \exp\{g_i[t]\}) \tag{12}$$

A.5.2 Derivation of GLM log-likelihood objective function (equation (5))

When fitting optimal GLM parameters for the ith RGC, the spikes from the coupled RGCs $\mathbf{s}_{\{i\}^C}[0, \ldots, T]$ are observed and known, and the spikes for RGC i that occur before time N $s_i[0, \ldots, N-1]$ are also known. The optimal GLM parameters for the ith RGC $\mathbf{m}_i, h_i, f_i, c_i^{(j)}$, and b_i can be found by minimizing the negative log-likelihood (negative of equation (12)) over the parameters. The negative log-likelihood can be simplified using the chain rule:

$$
\begin{aligned}
&- \log p(s_i[N,\ldots,T] \mid \mathbf{x}, s_i[0,\ldots N-1], \mathbf{s}_{\{i\}^C}[0,\ldots,T]) \\
&= -\sum_{t=N}^{T} \log p(s_i[t] \mid \mathbf{x}, s_i[0,\ldots,t-1], \mathbf{s}_{\{i\}^C}[0,\ldots,t-1]) \\
&= \sum_{t=N}^{T} \big\{ \log(1+\exp\{g_i[t]\}) - s_i[t] g_i[t] \big\},
\end{aligned}
$$

which results in the expression presented in (5).

A.5.3 Regularized GLM objective function

To reduce the number of GLM model parameters, the stimulus time filter $h_i[t]$, feedback (spike history) filter $f_i[t]$, and the neighboring cell coupling filters $c_i^{(j)}[t]$ were represented in terms of a small number of cosine bump basis vectors [10] (basis functions discussed in more detail in A.5.4). Letting B_h, B_f, and B_c represent the basis matrices for stimulus time, feedback, and coupling filters, respectively, the full time-domain filters can be recovered from the low dimensional representations $\mathbf{h}_i = B_h \tilde{\mathbf{h}}_i$, $\mathbf{f}_i = B_h \tilde{\mathbf{f}}_i$, and $\mathbf{c}_i^{(j)} = B_c \tilde{\mathbf{c}}_i^{(j)}$.

Substituting these low-dimensional temporal filters into the encoding negative log-likelihood from equation (5) yields an expression for that is jointly convex in $\{\mathbf{m}_i, \tilde{\mathbf{f}}_i, \tilde{\mathbf{c}}_i^{(j)}, b_i\}$ and in $\{\tilde{\mathbf{h}}_i, \tilde{\mathbf{f}}_i, \tilde{\mathbf{c}}_i^{(j)}, b_i\}$ but not with the stimulus spatial filter $\mathbf{m}$ and stimulus temporal filter $\tilde{\mathbf{h}}_i$ together because of the space-time stimulus filter separability assumption. As with the LNP models, L1 sparsity and L2 prior regularization terms were added. In addition, to eliminate spurious cell-cell correlations, an $L_{2,1}$ group-sparsity term was added to constrain the neighboring cell coupling filters $\tilde{\mathbf{c}}_i^{(j)}, b_i$. Because of the joint convexity issue described above, we fitted GLMs by alternating between solving two convex minimization problems:

$$
\begin{aligned}
\arg \min_{\mathbf{m}_i, \tilde{\mathbf{f}}_i, \tilde{\mathbf{c}}_i^{(j)}, b_i} \Big\{ &- \log p(s_i[N,\ldots,T \mid \mathbf{x}, s_i[0,\ldots,N-1], \mathbf{s}_{\{i\}^C}[0,\ldots,T]) \\
&+ \gamma_1 |\mathbf{m}_i|_1 + \frac{\gamma_2}{2} |\mathbf{m}_i - \mathbf{m}_i'|_2^2 + \gamma_3 \sum_j |\tilde{\mathbf{c}}_i^{(j)}|_2 \Big\},
\end{aligned}
$$

and

$$
\arg \min_{\tilde{\mathbf{h}}_i, \tilde{\mathbf{f}}_i, \tilde{\mathbf{c}}_i^{(j)}, b_i} \Big\{ - \log p(s_i[N,\ldots,T \mid \mathbf{x}, s_i[0,\ldots,N-1], \mathbf{s}_{\{i\}^C}[0,\ldots,T]) + \gamma_3 \sum_j |\tilde{\mathbf{c}}_i^{(j)}|_2 \Big\}.
$$

Each of the problems were solved using FISTA [26] with the proximal operator for the $L_{2,1}$ penalty from [29].

A.5.4 GLM time basis functions

Proper selection of temporal basis functions for the stimulus time filter, spiking feedback filter, and coupling filters is necessary for well-fitted GLM models. As in [10], basis functions corresponding to the first lobe of

$$
b^{(l)}[t] = \frac{1}{2} \cos(a \log[t+c] - \phi_l) + \frac{1}{2} \tag{13}
$$

were used. The quantities, a, c, and ϕ_l, as well as the number of basis functions used are hyperparameters. Because the GLM was fit with a 1 ms bin width and the filters were 250 samples long, t takes values $0, 1, ..., 249$. The paper used the following basis hyperparameters:

- For the stimulus time filter, $a = 5.5$, $c = 1.0$, and 10 total basis functions were used, corresponding to $\phi_l \in \{\frac{8\pi}{2}, \frac{9\pi}{2}, ..., \frac{16\pi}{2}, \frac{17\pi}{2}\}$.

- For the feedback filter, $a = 5.5$, $c = 1.0$, and 18 total basis functions were used, corresponding to $\phi_l \in \{0, \frac{\pi}{2}, ..., \frac{16\pi}{2}, \frac{17\pi}{2}\}$.

- For the coupling filter, $a = 3.2$, $c = 1.0$, and 10 total basis functions were used, corresponding to $\phi_l \in \{0, \frac{\pi}{2}, ..., \frac{9\pi}{2}\}$.

The basis set for the stimulus time filter was uniformly shifted backward in time to approximately match each retina's response latency to the stimulus.

A.5.5 Derivation of the total encoding log-likelihood term (equation (6))

The log-likelihood of the spike trains of all of the RGCs given the stimulus image and the spikes occurring prior to presentation of the stimulus can be computed using the chain rule. In particular, the total log-likelihood over all of the cells corresponding to time bin t

$$\log p(\mathbf{s}[t] \mid \mathbf{x}, \mathbf{s}[0, \ldots, t-1]) = \sum_{i \in \text{cells}} \log p(s_i[t] \mid \mathbf{x}, s_i[0, \ldots, t-1], \mathbf{s}_{\{i\}^C}[0, \ldots, t-1])$$

can be computed simply by summing over the cells, since the spiking responses in time bin t for each cell are independent of the other cells given the image and the spike histories for every cell up until time $t-1$. The overall log-likelihood corresponding to time bins $N, N+1, ..., T$ can then be computed using the chain rule

$$\begin{aligned}\log p(\mathbf{s}[N, ..., T] \mid \mathbf{x}, \mathbf{s}[0, ..., N-1]) &= \sum_{t=N}^{T} \log p(\mathbf{s}[t] \mid \mathbf{x}, \mathbf{s}[0, ..., t-1]) \\ &= \sum_{t=N}^{T} \sum_{i \in \text{cells}} \log p(s_i[t] \mid \mathbf{x}, s_i[0, ..., t-1], \mathbf{s}_{\{i\}^C}[0, ..., t-1])\end{aligned}$$

A.6 Initialization of HQS for MAP-GLM-dCNN method

We tested different methods of initializing $\mathbf{z}^{(1)}$ in Algorithm 1 for the MAP-GLM-dCNN. We compared initialization with the linear solution (as used for all results shown in the main text), with Gaussian noise initialization with standard deviations $\sigma \in \{10^{-4}, 10^{-3}, 10^{-2}, 10^{-1}, 1.0\}$, where images are defined on the interval $[-1, 1]$. Example test reconstructions for each initialization are shown in Figure 4, and mean test MS-SSIM and PSNR values for each initialization method are summarized in Tables 6 and 7. Qualitatively, the content and structure of the reconstructions did not show significant dependence on the initialization (with exception of the horizontal antenna of the insect in row C). However, the mean luminance of the image reconstructions did depend on the initialization method. Specifically, initialization with the linear solution tended to better recover the mean luminance (rows C, J, N) in cases where the stimulus image was particularly bright or particularly dark. Quantitatively, mean test and heldout MS-SSIM was largely independent of the initialization method (Table 6), while PSNR was worse for the randomly-initialized reconstructions (Table 7).

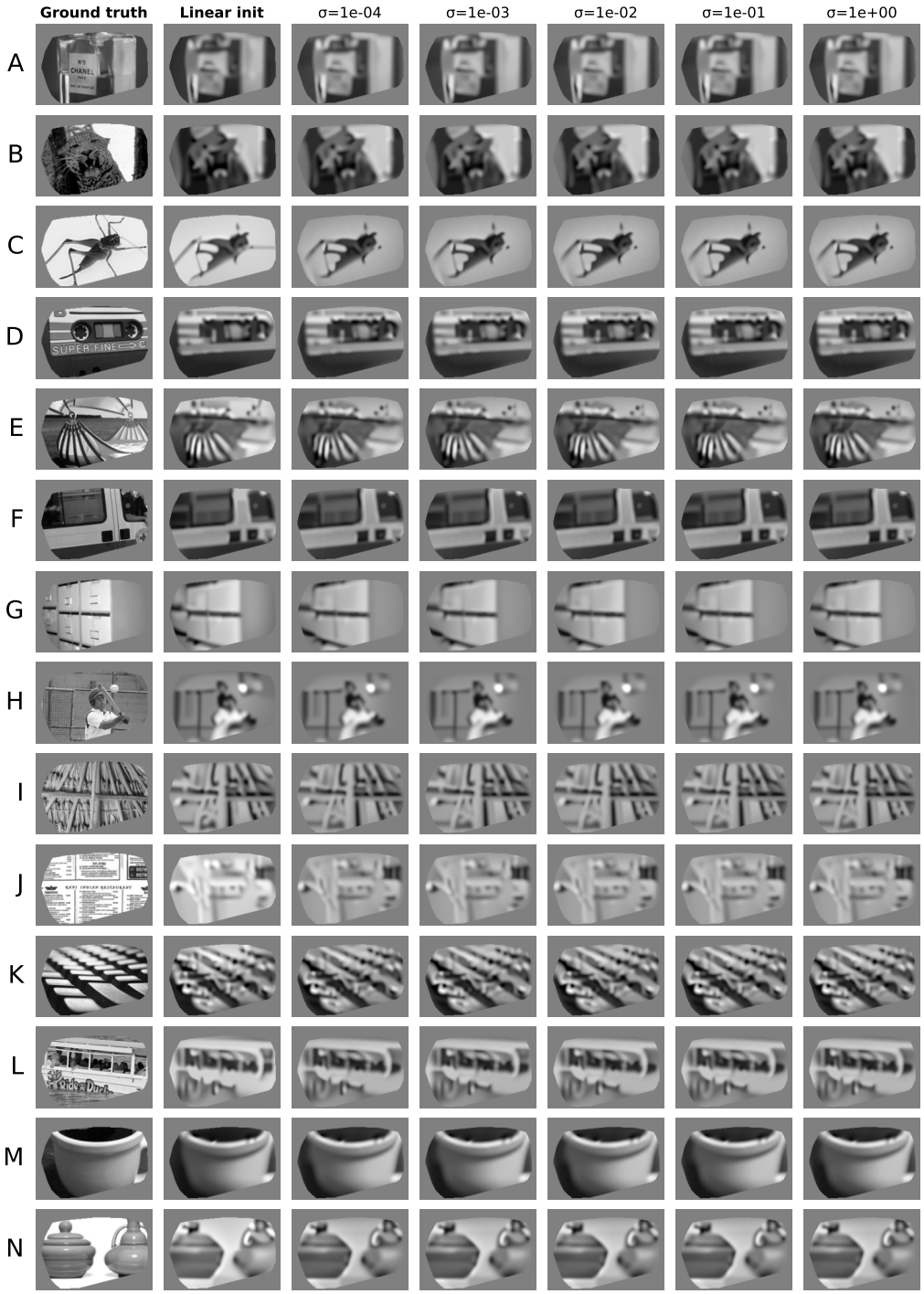

Figure 4: Example MAP-GLM-dCNN reconstructed images for the different initialization methods for $\mathbf{z}^{(1)}$ in Algorithm 1. Column contents: (1) Ground truth stimulus image; (2) Initialization with the linear solution, the method used in the main text; (3) random Gaussian initialization with $\sigma = 10^{-4}$; (4) random Gaussian initialization with $\sigma = 10^{-3}$; (5) random Gaussian initialization with standard deviation $\sigma = 10^{-2}$; (6) random Gaussian initialization with $\sigma = 10^{-1}$;, (7) random Gaussian initialization with $\sigma = 1$. All of the σ-values are defined for images that lie within the interval $[-1, 1]$.

Table 6: Average test and heldout MS-SSIM for each initialization method, for MAP-GLM-dCNN reconstruction. Initialization with the linear solution, the method presented in the main text, is bolded.

	Linear sol.		$\sigma = 10^{-4}$		$\sigma = 10^{-3}$		$\sigma = 10^{-2}$		$\sigma = 10^{-1}$		$\sigma = 1$	
	test	held	test	held	test	held	test	held	test	held	test	held
Retina 1	**0.689**	**0.688**	0.685	0.680	0.685	0.680	0.685	0.680	0.685	0.680	0.685	0.680
Retina 2	**0.668**	**0.673**	0.666	0.670	0.666	0.670	0.666	0.670	0.666	0.670	0.666	0.670

Table 7: Average test and heldout PSNR for each initialization method, for MAP-GLM-dCNN reconstruction. Initialization with the linear solution, the method presented in the main text, is bolded.

	Linear sol.		$\sigma = 10^{-4}$		$\sigma = 10^{-3}$		$\sigma = 10^{-2}$		$\sigma = 10^{-1}$		$\sigma = 1$	
	test	held	test	held	test	held	test	held	test	held	test	held
Retina 1	**19.5**	**19.6**	18.8	18.9	18.8	18.9	18.8	18.9	18.8	18.9	18.8	18.9
Retina 2	**18.5**	**18.5**	18.3	18.3	18.3	18.3	18.3	18.3	18.3	18.3	18.3	18.3

A.7 Implementation details for L-CAE and performance on experimental data

We used the published L-CAE model architecture [8]. This consisted of a linear regression decoder with parameters fitted by solving the normal equations, followed by a 4-layer convolutional encoder and 4-layer convolutional decoder to improve the linear reconstructions. The convolutional encoder and decoder were trained with backpropagation using a masked MSE loss (including only the regions of the image covered by recorded RGCs), the Adam optimizer [53] with learning rate $4 \cdot 10^{-3}$, and batch size 32. The number of training epochs was determined by evaluating the masked MSE loss on the test partition of the dataset.

The results in [8] were based on simulated RGC responses, and to our knowledge there are no published examples applying the L-CAE technique to experimentally recorded data. To verify that the L-CAE performs well with experimental data, we compared the performance of L-CAE and linear regression on the test partition (Figure 5). As expected, the L-CAE systematically produces improved PSNR, relative to linear regression. It also produces more perceptually accurate image reconstructions.

A.8 Implementation details for Kim *et al.* linear/nonlinear regression benchmark

The Kim *et al.* paper [4] reconstructs images from RGC spikes by breaking up the problem into three sequential *ad hoc* steps. The target image is decomposed into low spatial frequency and high spatial

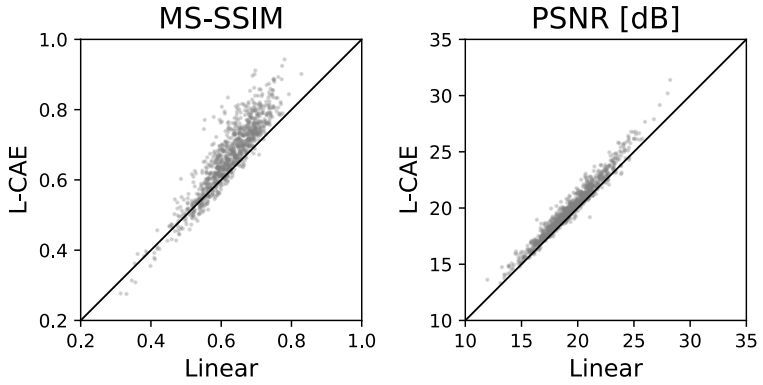

Figure 5: Performance of the L-CAE vs. linear reconstruction on the test partition of the experimental dataset for retina 1, demonstrating that the L-CAE technique can be applied effectively to experimental data. The L-CAE produced systematically greater MS-SSIM than linear reconstruction, suggesting that the L-CAE improves the perceptual similarity to ground truth of the reconstructions. The L-CAE also produced systematically better PSNR than linear reconstruction, which is expected since the L-CAE was trained with an MSE loss.

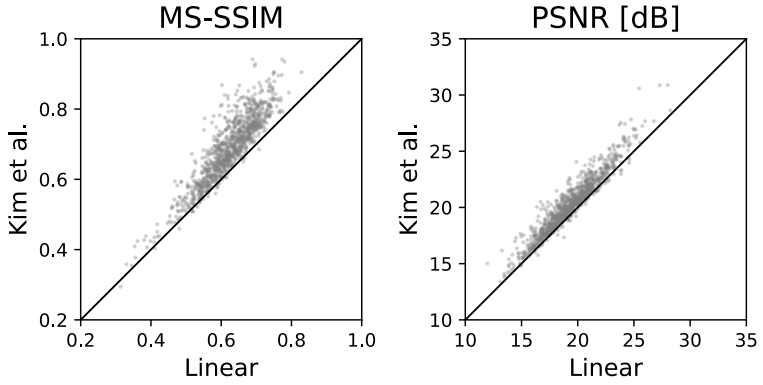

Figure 6: Performance of the Kim *et al.* method vs. linear reconstruction on the test partition of the experimental dataset for retina 1, validating our re-implementation.

frequency components. The low-frequency component is reconstructed using learned reconstruction filters, while the high-frequency component is reconstructed using a trained fully-connected neural network mapping the responses of the most relevant RGCs to the desired high-frequency pixel values. Finally, the low-frequency and high-frequency components are summed together and passed through a deblurring network with an architecture based on that of DeblurGANv2 [54].

The linear reconstruction filter was fitted by solving an L1-regularized linear-least-squares problem aiming to reconstruct the low-frequency image component, where the L1 hyperparameter was chosen by performing a grid search and evaluating MSE on the test partition. Cell/variable selection for the pixel-wise high-frequency component neural network was done by performing a separate L1-regularized linear-least-squares problem aiming to reconstruct the *full* image, with the L1 hyperparameter again chosen using grid search on the test partition. As in the published paper, the top 25 RGCs for each pixel were selected as inputs to the pixel-wise high-pass neural networks by taking the cells with the largest absolute reconstruction filter value for each respective pixel. The high-frequency neural networks were trained with using backpropagation with an MSE loss with respect to the high-frequency component of the target image. The DeblurGANv2 final deblur network was trained using backpropagation with an L1 loss with respect to the target image as well as an L1 perceptual similarity loss computed using the VGG [55] network.

To verify our implementation of the Kim *et al.* method, we compared reconstruction quality for images produced using this method against linear regression (Figure 6). As expected, Kim *et al.* systematically produces better MS-SSIM and PSNR than linear regression.

Checklist

1. For all authors...
   (a) Do the main claims made in the abstract and introduction accurately reflect the paper's contributions and scope? [Yes]
   (b) Did you describe the limitations of your work? [Yes] We have made comparisons to the appropriate benchmarks, and have described how the particular image reconstruction task differs from true natural vision.
   (c) Did you discuss any potential negative societal impacts of your work? [Yes] Potential positive impacts of the work regarding retinal prostheses for treating blindness are discussed in the third paragraph of the Discussion section 5. Because the work is specific to the retina, the negative impacts are limited and discussed in the Appendix A.1
   (d) Have you read the ethics review guidelines and ensured that your paper conforms to them? [Yes]
2. If you are including theoretical results...
   (a) Did you state the full set of assumptions of all theoretical results? [N/A]
   (b) Did you include complete proofs of all theoretical results? [N/A]
3. If you ran experiments...
   (a) Did you include the code, data, and instructions needed to reproduce the main experimental results (either in the supplemental material or as a URL)? [Yes] Code and fitted models are provided in the supplemental material, and a small subset of the experimental dataset used to generate the example figures is also provided.
   (b) Did you specify all the training details (e.g., data splits, hyperparameters, how they were chosen)? [Yes] Descriptions of hyperparameters and how they were selected are discussed in the methods. The train/test/heldout data partitions and descriptions of the datasets are provided in Tables 4 and 5, respectively.
   (c) Did you report error bars (e.g., with respect to the random seed after running experiments multiple times)? [N/A]
   (d) Did you include the total amount of compute and the type of resources used (e.g., type of GPUs, internal cluster, or cloud provider)? [Yes] Mentioned in the Appendix
4. If you are using existing assets (e.g., code, data, models) or curating/releasing new assets...
   (a) If your work uses existing assets, did you cite the creators? [Yes]
   (b) Did you mention the license of the assets? [No]
   (c) Did you include any new assets either in the supplemental material or as a URL? [Yes]
   (d) Did you discuss whether and how consent was obtained from people whose data you're using/curating? [N/A]
   (e) Did you discuss whether the data you are using/curating contains personally identifiable information or offensive content? [N/A]
5. If you used crowdsourcing or conducted research with human subjects...
   (a) Did you include the full text of instructions given to participants and screenshots, if applicable? [N/A]
   (b) Did you describe any potential participant risks, with links to Institutional Review Board (IRB) approvals, if applicable? [N/A]
   (c) Did you include the estimated hourly wage paid to participants and the total amount spent on participant compensation? [N/A]